Article

Design of MXene-Based Multiporous Nanosheet Stacking Structures Integrating Multiple Synergistic SERS Enhancements for Ultrasensitive Detection of Chloramphenicol

Yusi Peng, Lili Yang, Yanyan Li, Weida Zhang, Meimei Xu, Chenglong Lin, Jianjun Liu, Zhengren Huang,* and Yong Yang*

Read Online

ACCESS | 📊 Metrics & More | 📖 Article Recommendations | 🆂🅸 Supporting Information

ABSTRACT: Motivated by the desire for more sensitivity and stable surface-enhanced Raman scattering (SERS) substrates to trace detect chloramphenicol due to its high toxicity and ubiquity, MXene has attracted increasing attention and is encountering the high-priority task of further observably improving detection sensitivity. Herein, a universal SERS optimization strategy that incorporates NH_4VO_3 to induce few-layer MXenes assembling into multiporous nanosheet stacking structures was innovatively proposed. The synthesized Nb_2C-based multiporous nanosheet stacking structure can achieve a low limit of detection of 10^{-10} M and a high enhancement factor of 2.6×10^9 for MeB molecules, whose detection sensitivity is improved by 3 orders of magnitude relative to few-layer Nb_2C MXenes. Such remarkably enhanced

SERS sensitivity mainly originates from the multiple synergistic contributions of the developed physical adsorption, the chemical enhancement, and the conspicuously improved electromagnetic enhancement arising from the intersecting MXenes. Furthermore, the improved SERS sensitivity endows Nb_2C-based multiporous structures with the capability to achieve ultrasensitive detection of chloramphenicol with a wide linear range from 100 μg/mL to 1 ng/mL. We believe it is of great significance in conspicuously developing the SERS sensitivity of other MXenes with surficial negative charges and has a great promising perspective for the trace detection of other antibiotics in microsystems.

KEYWORDS: MXene, SERS optimization strategy, multiporous nanosheet stacking structure, trace detection of CAP
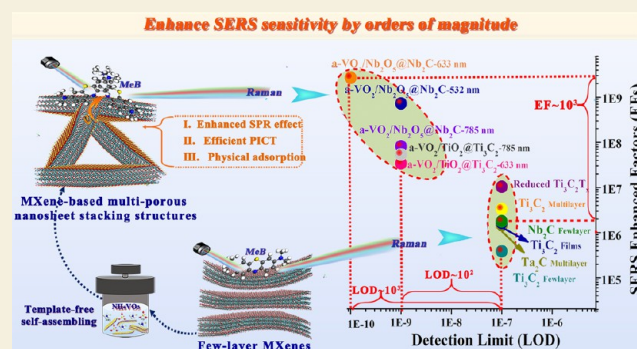
1. INTRODUCTION

Since the discovery of surface-enhanced Raman scattering (SERS), it has developed into an on-site rapid and ultra-sensitive trace detection technology with the vibration fingerprint characteristic, which is extensively applied in various fields of biosensing, environmental analysis, and food safety.[1] In recent years, with the significant increase of antibiotic drug abuse, food safety has aroused widespread concern in society. Chloramphenicol (CAP), as a broad-spectrum antibacterial drug, is frequently used illegally in aquaculture and agricultural animals and potentially enters the food chain because of its high efficacy against some bacterial diseases, affordability, and availability.[2] However, serious adverse reactions including barrier anemia, fatal aplastic anemia, leukemia, bone marrow suppression, optic neuritis, and headache can be caused to human health due to the residue of CAP in meat foods,[3,4] leading many countries to ban the use of CAP in food-producing animals. Therefore, it is necessary for human health to monitor the residual level of CAP in food-producing animals. Some common detection

methods of the CAP antibiotic including ELISA[5] and liquid chromatography−mass spectrometry (LC−MS)[6] still exhibit several limitations of having high cost and cumbersome operation and being time-consuming. In this regard, SERS technology with the advantages of being sensitive, fast, portable, and nondestructive has been developed for the detection of the CAP antibiotic in food and the environment. Recent publications have reported that noble metal nanoparticles with different morphologies of waffle-like AAO/Ag nanostructures[7] and Au/Ag-TiO$_2$ heterostructures[8] were developed to SERS detect the CAP antibiotic, all of which show the trace-level limit of detection (LOD). In order to promote the portable and practical development of SERS
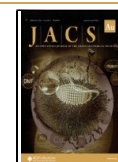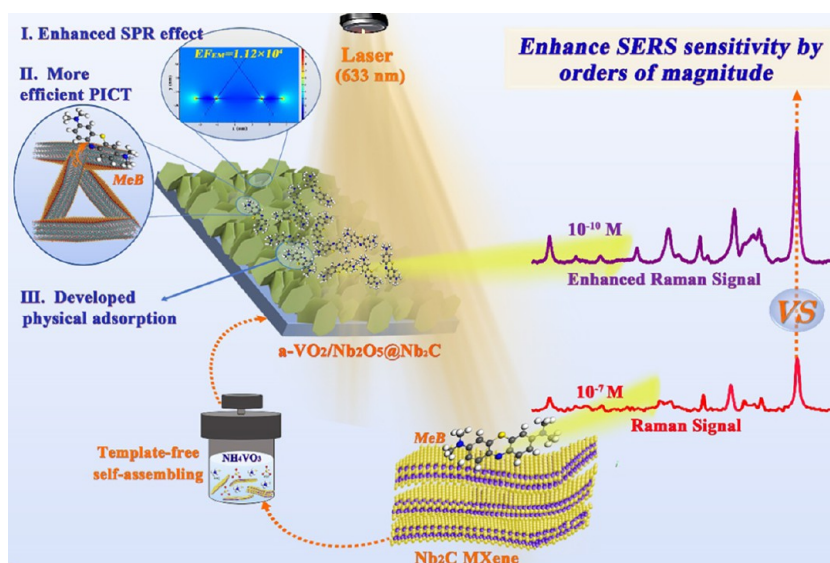
Figure 1. Schematic diagram of SERS-enhanced effects of MXene-based multiporous nanosheet stacking structure substrates.

technology, universal flexible SERS sensors of Au nano-triangles@PDMS and Au nanostars@PMMA films were applied for rapid detection of CAP in food samples with a low LOD of 3.41×10^{-11} M.[5,9] Furthermore, SERS nanotages based on magnetic nanoparticles were developed to achieve the enrichment and ultrasensitive detection of CAP in the complex environment with LOD down to the pg/mL level.[10,11] A vast array of research on the SERS detection of the CAP antibiotic has proved the feasibility and application potential of SERS technology for monitoring antibiotics in food and the environment.

Fundamentally, the pivotal research objective receiving the most attention regarding SERS technology is developing ultrasensitive and stable enhanced substrates for achieving trace SERS detection of CAP molecules. It is well acknowledged that electromagnetic enhancement (EM) and chemical enhancement (CM) are the most well-established enhancement mechanisms of Raman signals enhanced by SERS substrates.[12−15] Integration of the multiple contributions of CM and EM into nonmetallic SERS substrates may be a promising approach to significantly improve SERS sensitivity. As atomically thin semimetallic 2D materials, MXenes exhibit many fascinating properties such as conductivity, tunable electronic structure, high carrier mobility, high electronic density of states near the Fermi level, and the ability to achieve strong light−matter interaction at mid-infrared and THZ frequencies,[16−21] which is expected to endow MXenes with excellent SERS performance. For instance, the monolayer Ti_3C_2 nanosheets with high crystallinity synthesized by the Xi group exhibit excellent SERS performance with a LOD of 10^{-11} M and a high enhancement factor (EF) of 10^8, which is superior to most pure semiconductor-based SERS substrates reported at that time.[22] Additionally, the Ti_2N MXene film reported by George's group also exhibits outstanding SERS sensitivity, demonstrating the previous inference that MXenes as a semimetallic material can be utilized for ultrasensitive SERS substrates.[23] In our previous research, we reported for the first time two novel SERS substrates of Nb_2C and Ta_2C MXenes with LODs of 10^{-8} and 10^{-7} M, respectively.[24,25] Their SERS sensitivity is significantly lower than that of most semiconductors and also far weaker than the reported SERS

sensitivity of monolayer high-crystalline Ti_3C_2 nanosheets (as shown in Figure S1).[26−28] This abnormal conclusion is contrary to the inference of the ultrahigh SERS sensitivity of MXenes caused by their metallic property, which severely limits the practical application of MXenes in the SERS detection field. Therefore, developing a universal experimental strategy to significantly optimize the SERS sensitivity is a high-priority task for 2D MXene-based SERS substrates.

Based on the morphology analysis of the Ti_3C_2, Nb_2C, and Ta_2C MXenes prepared in the previous work, it is discovered that the MXene nanosheets synthesized by HF etching are seriously stacked along the (001) crystal plane due to the attraction of the van der Waals force, thus resulting in a larger thickness of MXene nanosheets. At this time, the advantages of 2D materials with large BET surface areas are lost for MXene nanosheets. A recent research study has fully proved that adjusting the morphology of Nb_2O_5 nanoparticles into Nb_2O_5 microflowers formed by the ultrathin nanosheets can significantly increase the BET surface area to provide more adsorption sites for probe molecules,[29] thereby improving its SERS sensitivity by an order of magnitude. Additionally, constructing a porous micronanostructure with a high BET surface area can not only exhibit the excellent adsorption capacity for probe molecules but also generate the strong local surface plasmon resonance (LSPR) effect and the high-density hotspot effect to further develop the SERS performance of substrates.[30,31] The above experimental strategy for constructing porous micronanostructures has been successfully extended to various nitride SERS substrates such as VN, MoN, WN, TiN, etc.[32,33] Furthermore, the highly ordered microcrystal structure assembled by ultrathin and oxygen vacancy-rich $W_{18}O_{49}$ nanowires with a thickness of about 1.5 nm simultaneously exhibits the conspicuously enhanced LSPR effect and the efficient interfacial charge transfer between substrates and molecules, thus successfully achieving an ultralow LOD of 10^{-11} M.[34] Assembling the uniform MoN and Mo_2C nanoparticles with a size of 2−5 nm into hollow spheres with a large surface area can achieve a strong LSPR effect in the visible region.[35] Similarly, V_2O_5 nanoparticles with a double-shelled hollow structure can not only realize the resonance absorption originated from the charge transfer and
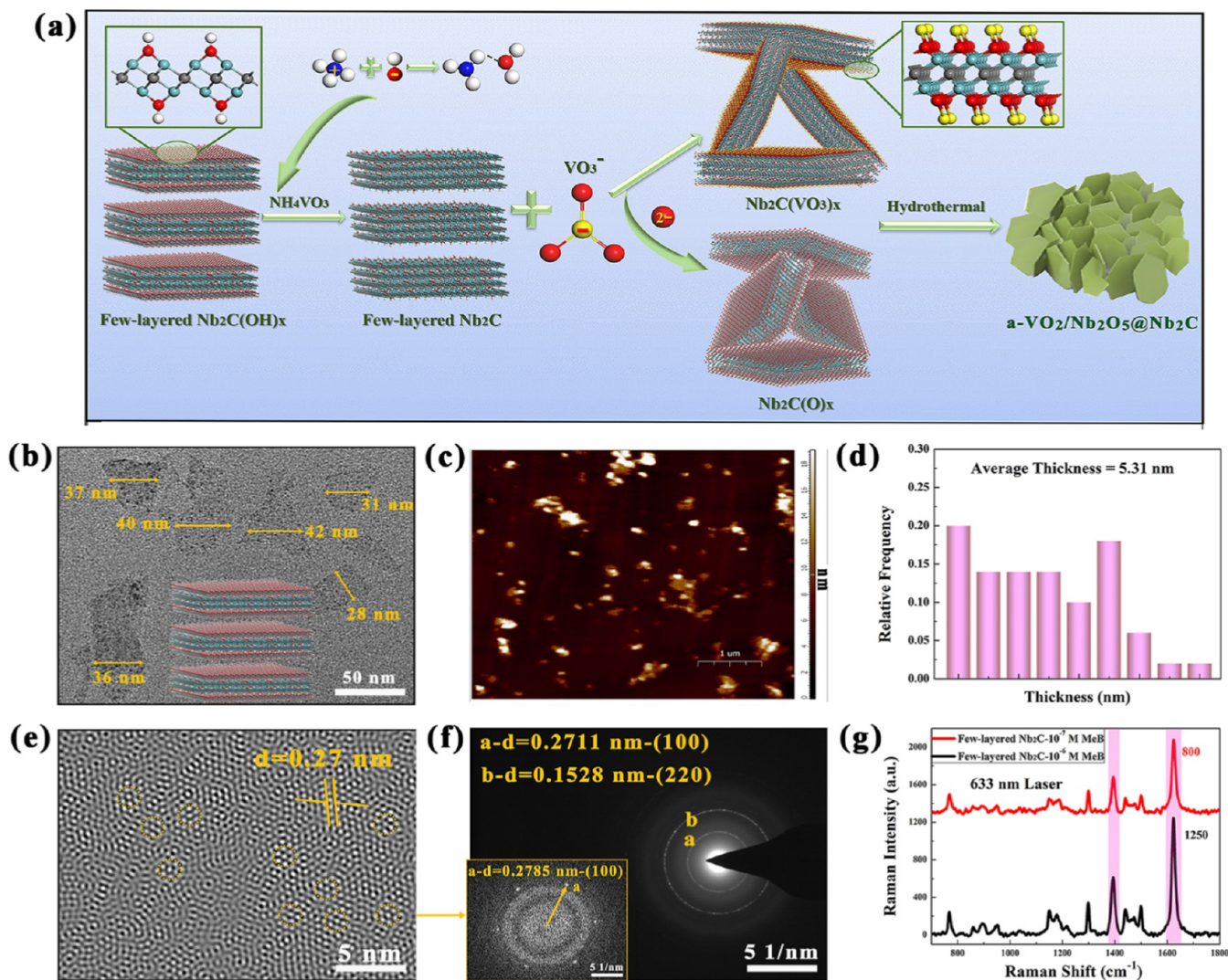
Figure 2. Experimental design of MXene-based multiporous nanosheet stacking structures and morphology characterization of few-layer Nb_2C MXene nanosheets. (a) Schematic diagram of the experimental design for MXene-based multiporous nanosheet stacking structures. (b) High-magnification TEM image. (c, d) AFM image and their thickness statistical histogram. (e) HRTEM image and (f) its corresponding SAED images. (g) Raman spectra of $10^{-6}-10^{-7}$ M MeB on few-layer Nb_2C nanosheets.

exciton enhancements but also achieve the coupling effect of electromagnetic enhancement due to the nanostructure of the inner and outer shells.[36] The aforementioned research has fully demonstrated that reassembling the smaller-sized nanoparticles into complex nanostructures with a regular morphology is an effective experimental strategy to improve the SERS sensitivity of materials by enhancing the LSPR effect. With regard to semiconductor substrates, the SERS enhancement mainly arises from the enhanced chemical bond vibration of molecules caused by the charge transfer between substrates and molecules. Currently, a large number of literature studies have confirmed that the amorphization of SERS substrates is able to conspicuously increase the excited electrons near the Fermi level, thereby developing the chemical enhancement effect of semiconductor materials on probe molecules.[37−40] Hence, forming a uniform amorphous layer on the surface of crystalline MXene nanosheets may be an efficient method to further improve the SERS detection sensitivity. In conclusion, the combination of 3D assembling and amorphizing MXene nanosheets is expected to synergistically improve the SERS performance of MXenes from three aspects of physical

enrichment, CM, and EM and thus propose a universal experimental strategy that can conspicuously optimize the SERS sensitivity of MXenes.

In this work, aiming for the objective of observably developing SERS sensitivity for MXenes to achieve trace detection of CAP, we developed a universal optimization strategy of SERS performance that assembled few-layer MXene nanosheets into multiporous nanosheet stacking structures to improve the detection sensitivity of MXenes by orders of magnitude (Figure 1). Taking Nb_2C MXene nanosheets as an example, the synthesized multiporous nanosheet stacking structures with a micrometer scale of about 5 μm are composed of Nb_2C MXenes with an average thickness of about 5.8 nm intersecting each other, and their phase structure is determined to be a-VO_2/Nb_2O_5@Nb_2C. The a-VO_2/Nb_2O_5@Nb_2C multiporous nanosheet stacking structures as SERS substrates can be effectively excited by the irradiation laser of the entire visible region to achieve excellent detection sensitivity for MeB molecules with a low LOD of 10^{-10} M and a high EF of 2.6×10^9, whose SERS sensitivity is improved by at least 3 orders of magnitude relative to few-layer Nb_2C

MXene nanosheets. The improved SERS performance is mainly determined from three perspectives, namely, physical enrichment, chemical enhancement, and electromagnetic enhancement. Finally, other MXene nanosheets are applied as assembling templates to verify the universality of this SERS optimization strategy, which paves a new path for conspicuously optimizing the SERS sensitivity of other 2D nanosheet substrates with surficial negative charges. Furthermore, ultrasensitive detection of CAP with a wide linear range from 100 μg/mL to 1 ng/mL was achieved by the developed Nb$_2$C-based multiporous nanosheet stacking structure, which has a great promising perspective for the trace detection of other antibiotics in microsystems.

2. RESULTS AND DISCUSSION

2.1. Design of the MXene-Based Multiporous Nanosheet Stacking Structure

Based on previous reports on MXene materials, it is discovered that the surface of MXene nanosheets synthesized by HF etching and tetrapropylammonium hydroxide (TPAOH) delamination is prone to adsorb a large number of −OH ions, thus showing surficial negative charges.[41] Moreover, these synthesized MXene nanosheets are seriously stacked along the (001) crystal plane due to the attraction of the van der Waals force, resulting in a larger thickness of MXene nanosheets without the advantages of large BET surface areas for 2D materials. Therefore, the key solution strategy of 3D assembling and surface amorphizing MXenes was adopted to destroy the van der Waals attraction between the MXene nanosheets that endowed MXenes with a stacked morphology, thereby increasing their BET surface area on the one hand and improving the electromagnetic enhanced factor contributed by surface plasmon enhancement on the other hand. The schematic diagram of this experimental design is shown in Figure 2a. Herein, the design fundamental is the full use of the −OH ions adsorbed on the surface of MXenes and its surficial negative charge. The few-layer MXene nanosheets were applied as assembly templates. The key of this experimental design is that the ammonium ions (NH^{4+}) with a positive charge generated by the hydrolysis of the incorporated ammonium metavanadate (NH$_4$VO$_3$) are capable of reacting with the hydroxide ions (OH$^-$) on the surface of MXenes to produce ammonia gas, thereby taking away the OH$^-$ ions of the MXene surface and providing more adsorption and reaction sites for the remaining metavanadate ions (VO$_3^-$). During the hydrothermal reaction, the few-layer MXene nanosheets will aggregate together due to the great surface energy, but the original van der Waals attraction existing in the MXene nanosheet layers will be destroyed due to the formation of amorphous oxide a-VO$_2$/M$_x$O$_y$ (M = Nb, Ti) on the surface of MXenes, further making the nanosheets intersect each other to grow into the MXene-based multiporous nanosheet stacking structure.

For the convenience of comparing SERS performance, Nb$_2$C MXenes were taken as an example to synthesize the MXene-based multiporous nanosheet stacking structure. Here, preparing the assembly templates of multiporous nanosheet stacking structures was the foremost task. Experimental methods of HF etching, TPAOH delamination, and ultrasonic vibration fragmentation were adopted to synthesize few-layer Nb$_2$C MXene nanosheets. First of all, the morphology of few-layer Nb$_2$C MXene nanosheets was analyzed by scanning

electron microscopy (SEM) and low-magnification transmission electron microscopy (TEM) images. As shown in Figure S2a,b, most MXenes present a uniform nanosheet structure and lie flat on the substrates. The high-magnification TEM image shown in Figure 2b also presents an electronically transparent nanosheet morphology, which further reflects the lateral dimensions of about 30−100 nm for the Nb$_2$C MXenes. Then, the thickness of the Nb$_2$C MXene nanosheets was characterized by atomic force microscopy (AFM) images (Figures 2c,d and S2c,d). It is found that the thickness of the synthesized Nb$_2$C MXene assembly templates is in the range of 3−10 nm, and the statistical average thickness is about 5.31 nm corresponding to the 10-layer Nb$_2$C nanosheets, which can be defined as few-layer Nb$_2$C MXene nanosheets. Additionally, the clear lattice fringes on Nb$_2$C MXenes are easily discerned by high-resolution TEM (HRTEM) and its corresponding selected area electron diffraction (SAED) images (Figure 2e,f), which correspond to the (100) and (003) planes of hexagonal structures with interplanar spacings of 0.271 and 0.435 nm, respectively. Notably, since these few-layer Nb$_2$C MXene nanosheets stack in different directions under the weak van der Waals attractions, their SAED images present sharp and bright diffraction rings arising from (100) and (220) planes of Nb$_2$C MXenes, indicating the excellent crystallinity of the synthesized few-layer Nb$_2$C MXene nanosheets. Furthermore, research on its SERS performance (Figures 2g and S3) indicates that the SERS enhancement of few-layer Nb$_2$C MXene nanosheets on MeB molecules can be more significantly excited by an irradiation laser of 633 nm, and the corresponding LOD and EF can reach 10^{-7} M and 1.72×10^6, respectively.

2.2. Synthesis and Characterization of the Nb$_2$C-Based Multiporous Nanosheet Stacking Structure

The aforementioned synthesized few-layer Nb$_2$C MXene nanosheets with high crystallinity were applied as assembly templates to synthesize Nb$_2$C-based multiporous nanosheet stacking structures by incorporating NH$_4$VO$_3$. For the convenience of qualitative comparisons, the SERS enhancements of these regulated synthesized substrates on MeB molecules are mainly applied as the evaluation standard. Here, the time and temperature of hydrothermal reactions and the concentration of few-layer Nb$_2$C MXene powder and NH$_4$VO$_3$ are sequentially adjusted, and the Raman spectra are shown in Figure S4. When the hydrothermal reaction time and temperature are controlled to be 6 h and 150 °C, respectively, as well as adding 0.02 g of few-layer Nb$_2$C MXenes powder and 0.75 g of NH$_4$VO$_3$ as reactants, the Nb$_2$C-based multiporous nanosheet stacking structures with the most regular morphology and the best SERS performance are obtained. Furthermore, SEM images are characterized to explore the regulation of the concentration of NH$_4$VO$_3$ on the morphology of products (Figure S5). It can be clearly seen that these few-layer Nb$_2$C MXenes are restacked together due to the van der Waals attraction between nanosheet layers when a small amount of NH$_4$VO$_3$ is added. As the addition amount of NH$_4$VO$_3$ gradually increases, the amorphous oxide layers are formed on the surface of more few-layer Nb$_2$C MXene nanosheets, thereby destroying the original van der Waals attraction between nanosheet layers. Hence, it is natural to make Nb$_2$C nanosheets intersect each other to grow into Nb$_2$C-based multiporous nanosheet stacking structures.

Here, Nb$_2$C-based multiporous nanosheet stacking structures were successfully synthesized by adjusting the hydro-
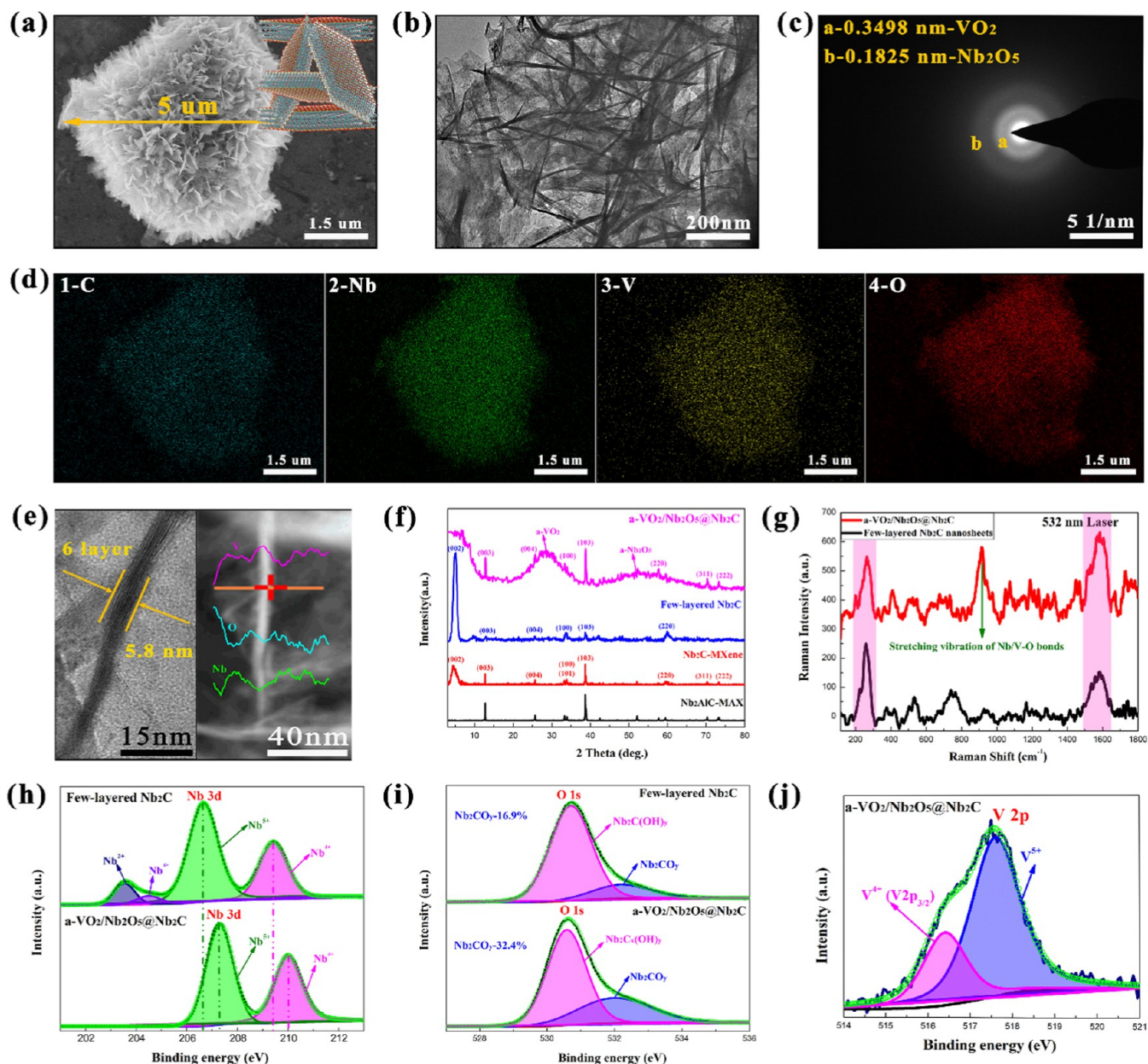
Figure 3. Morphology characterization and physical phase determination of Nb_2C-based multiporous nanosheet stacking structures. (a) SEM image. (b) TEM image. (c) The corresponding SAED image. (d) The element distribution mapping images of C, Nb, V, and O. (e) HRTEM image for the cross section of nanosheets composed of Nb_2C-based multiporous nanosheet stacking structures. (f) XRD patterns. (g) Raman spectra. (h−j) Nb 3d (h), O 1s (i), and V 2p (j) XPS spectra.

thermal reaction time, temperature, and the concentration of reactants. The low-magnification SEM image in Figure 3a shows that the lateral dimension of the as-synthesized Nb_2C-based multiporous nanosheet stacking structure is able to reach the micrometer scale of about 5 μm, while the corresponding high-magnification SEM image (Figure S6a) presents that Nb_2C MXene nanosheets exist in an interlaced morphology, and the roughly characterized thickness of nanosheets is in the range of 4−5 nm. Furthermore, the electron-transparent nanosheet structure and obvious wrinkled morphology formed by the intersecting nanosheets can also be clearly identified from the TEM image, as shown in Figure 3b. Its corresponding SAED image (Figure 3c) presents a diffuse amorphous diffraction ring arising from the amorphous oxides of Nb and V elements. The energy-dispersive spectroscopy (EDS)

(Figure S6b) exhibits the distinct signal of the V element in addition to the signals of Nb, C, and O elements, indicating the successful introduction of the V element. Then, the EDS element distribution of Nb_2C-based multiporous nanosheet stacking structures is further characterized and shown in Figure 3d. It can be easily found that Nb, C, V, and O elements are uniformly distributed on the surface of the entire Nb_2C-based multiporous nanosheet stacking structures, demonstrating the fact that the added VO_3^- ions are uniformly adsorbed on the surface of MXenes and participate in the hydrothermal reactions. The high-magnification TEM image in Figure 3e shows the cross-sectional morphology of Nb_2C nanosheets in a Nb_2C-based multiporous nanosheet stacking structure. It is discovered that the thickness of amorphous Nb_2C MXenes can reach 5.8 nm, corresponding to about six layers of stacked
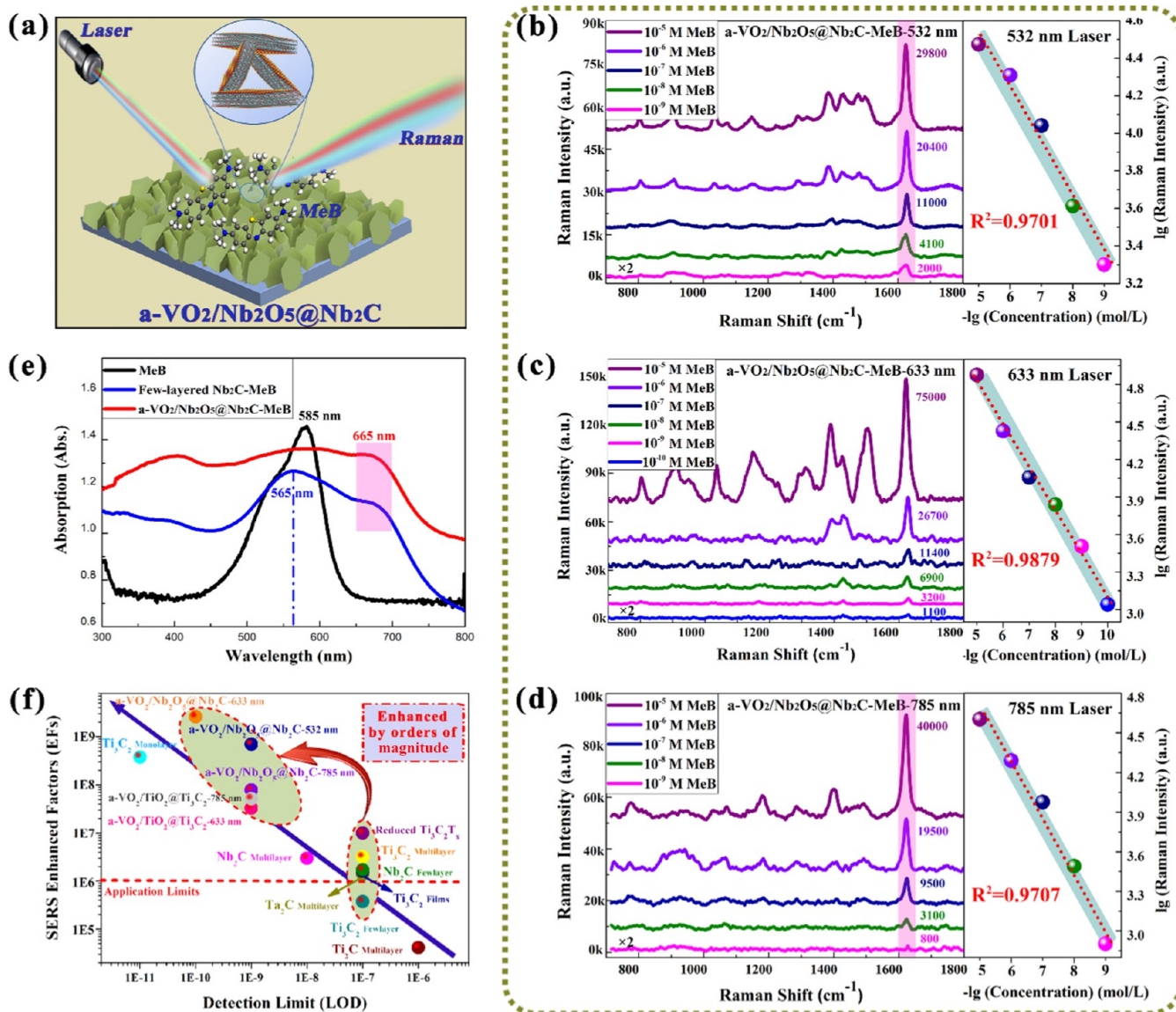
Figure 4. SERS performance of Nb₂C-based multiporous nanosheet stacking structures. (a) Raman scattering diagram of MeB molecules on multiporous nanosheet stacking structure substrates. (b–d) Raman spectra and linear relationship between Raman intensity and molecular concentration of MeB with a concentration range of $10^{-5}–10^{-10}$ M on Nb₂C-based multiporous nanosheet stacking structure substrates under the excitation lasers of 532 nm (b), 633 nm (c), and 785 nm (d). Their corresponding Raman intensity at 1620 cm^{-1} as a function of molecular concentrations. (e) Ultraviolet–visible spectra of the complexes between few-layer Nb₂C nanosheets or a-VO₂/Nb₂O₅@Nb₂C and MeB molecules. (f) Comparison of the SERS performance of the reported MXene-based substrates and the MXene-based multiporous nanosheet stacking structure in this work.

Nb₂C nanosheets, which is thicker than the thickness of 3.18 nm for the six layers of the stacked Nb₂C nanosheets before hydrothermal reactions, which is reasonable to speculate that it is presumably the contribution of amorphous oxide layers of Nb and V elements.

Then, the X-ray photoelectron spectroscopy (XPS), X-ray diffraction (XRD), and Raman characterization were carried out to analyze the phase structure and elemental chemical valence states of Nb₂C-based multiporous nanosheet stacking structures. Compared with the Nb 3d XPS peaks of few-layer Nb₂C MXene nanosheets, the Nb 3d peaks arising from Nb²⁺ and Nb⁴⁺ of multiporous nanosheet stacking structures located at 203.55 and 204.5 eV disappear, while the Nb 3d XPS peaks representing Nb⁵⁺ and Nb⁴⁺ shift from 206.65 and 209.4 eV to the higher binding energy of 207.25 and 210 eV (Figure 3h),

respectively, which indicates that the Nb elements exhibit a tendency to transform to a high valence state and the pentavalent oxides of partial Nb elements are formed. Furthermore, the analysis of O 1s XPS spectra (Figure 3i) reveals that the Nb₂C-based multiporous nanosheet stacking structures exhibit a higher oxide content relative to the few-layer Nb₂C MXene nanosheets. It can be ascribed to the fact that the few-layer Nb₂C MXene nanosheets are further oxidized during the process of hydrothermal reaction, which is demonstrated by the existence of amorphous V/Nb oxide in the SAED image. Additionally, the V 2p XPS peaks (Figure 3j) located at 516.4 and 517.6 eV are surprisingly detected, indicating that the V elements mostly exist in the valence state of V⁵⁺ in the Nb₂C-based multiporous nanosheet stacking structures, and a small part exists in the valence state of V⁴⁺.

The V elements with nonmonovalent states also demonstrate the existence of amorphous V oxides.

In order to further determine the phase structure of Nb_2C-based multiporous nanosheet stacking structures, XRD patterns were analyzed in detail (Figure 3f). It can be easily inferred that the multilayer Nb_2C MXenes are successfully synthesized by HF etching the Nb_2AlC MAX phase. The intensity of the (002) characteristic peak representing MXenes is significantly enhanced and shifts to a lower XRD diffraction angle after TPAOH exfoliation and ultrasonic oscillation treatment, which indicates the successful synthesis of a large number of few-layer Nb_2C MXene nanosheets with the larger interlayer spacing. The synthesized Nb_2C-based multiporous nanosheet stacking structures not only retain a set of sharp XRD characteristic peaks of Nb_2C MXene nanosheets but also generate the broadened XRD peaks at diffraction angles of around 30 and 55°, which belong to amorphous VO_2 and Nb_2O_5, respectively. Therefore, the phase structure of Nb_2C-based multiporous nanosheet stacking structures is determined to be a-VO_2/Nb_2O_5@Nb_2C, where amorphous a-VO_2/Nb_2O_5 exists on the surface of Nb_2C MXene nanosheets with excellent crystallinity, which is highly consistent with the analysis results of XPS and SAED. The analysis of Raman spectra (Figure 3g) demonstrates that Nb_2C-based multiporous nanosheet stacking structures retain the original Raman peaks of Nb_2C MXenes and simultaneously show a Raman peak at 913 cm^{-1}, representing the stretching vibration mode of Nb−O and V−O bonds, which demonstrates the successful introduction of V elements and the formation of Nb and V oxides, which are also consistent with the aforementioned characterization results.

2.3. SERS Performance of the Nb_2C-Based Multiporous Nanosheet Stacking Structure

Subsequently, the SERS performance of the synthesized a-VO_2/Nb_2O_5@Nb_2C multiporous nanosheet stacking structure was evaluated, and the Raman scattering diagram of MeB molecules on multiporous nanosheet stacking structure substrates is presented in Figure 4a. First, the optimal SERS excitation wavelength of a-VO_2/Nb_2O_5@Nb_2C substrates for MeB molecules was explored. As shown in Figure 4b−d, MeB molecules adsorbed on the a-VO_2/Nb_2O_5@Nb_2C substrates can be excited to produce significantly enhanced Raman signals under irradiation lasers of 532, 633, and 785 nm. Among them, the Raman spectra excited by the 633 nm laser exhibit an obviously stronger Raman enhancement, thus determining the optimal SERS excitation wavelength of 633 nm. The above phenomenon can be attributed to the fact that the strongest UV−vis absorption peak of a-VO_2/Nb_2O_5@Nb_2C-MeB complexes is located near 633 nm (Figure 4e). Under the excitation lasers of 532 and 785 nm, the LODs of a-VO_2/Nb_2O_5@Nb_2C substrates for MeB molecules can reach 10^{-9} M, and the corresponding EFs at 1620 cm^{-1} are 7.0 × 10^8 and 7.9 × 10^7, respectively, while under the optimal excitation laser of 633 nm, even if the MeB molecules are further diluted to a low molar concentration of 10^{-10} M, a distinct enhanced Raman signal is able to be detected by adsorbing MeB molecules on a-VO_2/Nb_2O_5@Nb_2C substrates. Therefore, the LOD of a-VO_2/Nb_2O_5@Nb_2C substrates with the excitation laser of 633 nm is determined to be 10^{-10} M, and the EF can be as high as 2.6 × 10^9. Compared to the LOD of 10^{-7} M and EF of 1.72 × 10^6 for the few-layer Nb_2C MXene nanosheets, the SERS sensitivity of a-VO_2/Nb_2O_5@Nb_2C substrates is

improved by 3 orders of magnitude, which is among the best in the reported pure MXene-based SERS substrates (Figure 4f and Table S1). Moreover, the corresponding relationship trends of Raman intensity at 1620 cm^{-1} changing with the concentration of MeB molecules under the excitation lasers of 532, 633, and 785 nm (Figure 4b−d) represent that their linear relationships are satisfactory in the range from 10^{-5} to 10^{-9} M or 10^{-10} M with the correlation coefficients of 0.9701, 0.9879, and 0.9707, respectively, which demonstrates the accuracy of Raman detected results. Here, the main Raman peaks of MeB molecules enhanced by a-VO_2/Nb_2O_5@Nb_2C substrates at 1620, 1502, and 1392 cm^{-1} are assigned to the asymmetric stretching vibration of the benzene ring and the asymmetric and symmetric C−N stretching vibrations (Table S2), respectively. Generally, Raman spectra of 10^{-9} M MeB molecules on a-VO_2/Nb_2O_5@Nb_2C substrates with 187 test points in an area of 80 × 50 μm^2 are scanned to characterize the uniformity of SERS enhancement, and the Raman mapping and the corresponding Raman intensity scatter plots are shown in Figure S7. The calculated relative standard deviations (RSDs) of Raman intensity at 445, 1395, and 1617 cm^{-1} are 12.0, 11.6, and 10.5%, respectively, indicating the excellent uniformity of SERS enhancement for a-VO_2/Nb_2O_5@Nb_2C substrates. In conclusion, the a-VO_2/Nb_2O_5@Nb_2C multiporous nanosheet stacking structures assembled by few-layer Nb_2C MXene nanosheets exhibit ultrasensitive SERS detection ability, which is superior to the majority of reported semiconductor-based SERS substrates to the best of our knowledge.

2.4. Validation of Universality for the Optimization Strategy

In order to verify the universality of this optimization strategy of assembling few-layer MXene nanosheets into MXene-based multiporous nanosheet stacking structures, stable Ti_3C_2 MXene nanosheets were selected as assembly templates to conduct the same hydrothermal reaction. As shown in Figure S8, the few-layer Ti_3C_2 MXene nanosheets with good crystallinity and about 70−150 nm lateral dimensions as well as about 16 nm thickness are synthesized. The LOD and EF of few-layer Ti_3C_2 MXene nanosheets for MeB molecules with the excitation laser of 633 nm are 10^{-7} M and 3.75 × 10^5, respectively. After the hydrothermal reaction with adding NH_4VO_3, the SEM and TEM images in Figure S10a,b demonstrate that Ti_3C_2-based multiporous nanosheet stacking structures with a lateral dimension in the micron scale are also successfully synthesized. The SAED image (Figure S10c) simultaneously shows diffused amorphous rings and crystalline diffraction spots, wherein the crystalline diffraction spots correspond to the (003), (220), and (311) planes of Ti_3C_2 MXenes with high crystallinity, while diffused amorphous rings correspond to the amorphous oxides of Ti and V. Compared with a-VO_2/Nb_2O_5@Nb_2C, it is discovered that as the size and thickness of MXene nanosheets increase, the morphology of this MXene-based multiporous nanosheet stacking structures becomes more regular. The nonmonovalent states of V^{5+} (516.4 eV) and V^{4+} (517.6 eV) are also presented in V 2p XPS spectra (Figure S10d) of Ti_3C_2-based multiporous nanosheet stacking structures, demonstrating the existence of amorphous V oxides. The phase structure of Ti_3C_2-based multiporous nanosheet stacking structures is further determined by the sharp XRD peaks of crystalline Ti_3C_2 MXene and the broadened XRD diffraction peaks of amorphous VO_2/TiO_2
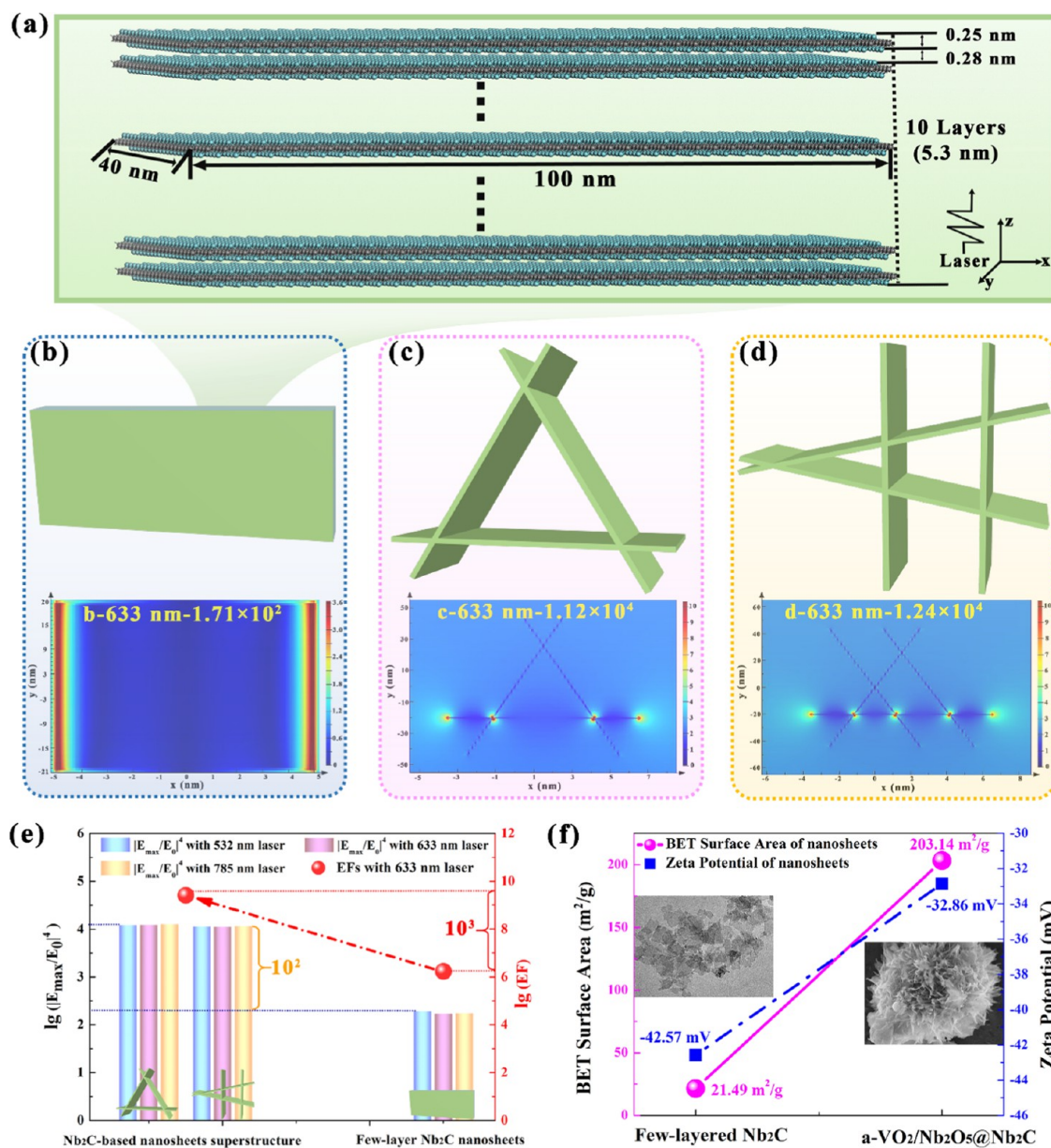
Figure 5. Contribution of electromagnetic enhancement for Nb$_2$C-based multiporous nanosheet stacking structures to SERS activity based on FDTD simulations. (a) Construction of the FDTD simulation model for single few-layer Nb$_2$C MXene nanosheets. (b−d) Simulated electric field intensity distribution and corresponding enhancement factors of the single few-layer Nb$_2$C MXene nanosheet model (b), regular triangular intersected Nb$_2$C MXene nanosheet model (c), and irregular intersected Nb$_2$C MXene nanosheet model (d) under the excitation of the TFSF light source at 633 nm. The color bar represents electric field intensity. (e) The electromagnetic enhancement factors ($|E|^4/|E_0|^4$) based on the FDTD method of the above three simulated models with three TFSF light sources of 532, 633, and 785 nm. The SERS EFs of MeB on few-layer Nb$_2$C nanosheets and Nb$_2$C-based multiporous nanosheet stacking structures. (f) ζ-potential and BET surface area of few-layer Nb$_2$C nanosheets and a-VO$_2$/Nb$_2$O$_5$@Nb$_2$C.

in XRD patterns (Figure S10e), that is, a-VO$_2$/TiO$_2$@Ti$_3$C$_2$. Accordingly, the successful synthesis of a-VO$_2$/TiO$_2$@Ti$_3$C$_2$ multiporous nanosheet stacking structures has verified the universality and feasibility of this experimental method, which can be extended to other MXene nanosheets with surficial negative charges.

Similarly, MeB molecules are also employed to evaluate the SERS performance of a-VO$_2$/TiO$_2$@Ti$_3$C$_2$. Raman spectra in Figure S11 indicate that when the concentration of MeB molecules is diluted to 10^{-9} M, the obvious Raman speaks of MeB molecules can be detected by adsorbing on a-VO$_2$/TiO$_2$@Ti$_3$C$_2$ substrates with the excitation lasers of 633 and

785 nm, in which the Raman signals are more significantly enhanced by the excitation laser of 785 nm. Moreover, their trends of Raman intensity with MeB concentrations of 10^{-5}−10^{-9} M exhibit excellent linear relationships with correlation coefficients of 0.9639 and 0,9759. Therefore, it is reasonable to confirm that the LOD and EF of a-VO$_2$/TiO$_2$@Ti$_3$C$_2$ substrates for MeB molecules with the excitation laser of 785 nm are determined to 10^{-9} M and 5.2 × 10^7, respectively, which are both improved by 2 orders of magnitude relative to the SERS sensitivity of few-layer Ti$_3$C$_2$ MXene nanosheets. Here, an interesting conclusion that the synthesized MXene-based multiporous nanosheet stacking structures can be

effectively excited by various wavelengths of the irradiation laser to generate outstanding SERS enhancement can be discovered. In conclusion, a universality optimization strategy of SERS performance, that is, assembling few-layer MXene nanosheets into multiporous nanosheet stacking structures, was proposed to develop its SERS sensitivity by orders of magnitude, which is of great significance in conspicuously developing the SERS sensitivity of other MXene materials with surficial negative charges.

2.5. SERS Enhancement Mechanism of the MXene-Based Multiporous Nanosheet Stacking Structure

Currently, research on the SERS performance of MXenes has indicated that their SERS enhancement mechanism mainly originates from the synergistic contribution of CM dominated by the PICT process and EM. Therefore, the exploration of the SERS enhancement mechanism for MXene-based multiporous nanosheet stacking structures is also mainly considered from the perspectives of CM and EM. First of all, the contribution of the existence of V/Nb amorphous oxides on the surface of Nb_2C MXenes to the chemical enhancement was investigated by density functional theory (DFT) calculations. The amorphous adsorption models of Nb_2CO_2 and Nb_2CO_2V were constructed, in which both −O and −VO_2 groups were located above C atoms and adsorbed on the surface of Nb_2C MXenes crystal structures by bonding with Nb atoms (Figure S12a). The calculated static Raman spectra (Figure S12b) of Nb_2C, Nb_2CO_2, and Nb_2CO_2V clusters on MeB molecules indicate that the presence of V/Nb amorphous oxide on the surface of nanosheets endows Nb_2C MXenes with the reduced static Raman enhancement of about an order of magnitude, which is contrary to the expectation that amorphizing materials could facilitate charge transfer to improve the static Raman enhancement. It could be attributed to the fact that there are a large number of unbounded active electrons on the surface of Nb_2C MXenes to conduce the static charge transfer with molecules, while the existence of amorphous oxides on the surface of MXenes instead localizes this part of active electrons, resulting in a decrease of static Raman enhancements. Additionally, the calculated density of electronic states, absorption spectrum, and dielectric function spectrum of Nb_2C, Nb_2CO_2 and Nb_2CO_2V amorphous adsorption models (Figure S12c−e) indicate that the electronic state density near the Fermi level of amorphous adsorption models is observably increased relative to Nb_2C MXenes. Moreover, the absorption peaks and the real part of dielectric functions of amorphous adsorption models still span the entire visible region, which is beneficial to promote the photoinduced charge transfers between substrates and molecules, thereby enhancing the dynamic Raman enhancements. Notably, the calculated absorption peaks spanning the entire visible region of Nb_2CO_2 and Nb_2CO_2V amorphous adsorption models are consistent with the experimental absorption peaks of a-VO_2/Nb_2O_5@Nb_2C shown in Figure S13. Therefore, although the existence of V/Nb amorphous oxide on the surface of Nb_2C MXenes will reduce the static Raman enhancement, it can destroy the original van der Waals attraction between MXene layers to form multiporous nanosheet stacking structures and simultaneously improve the dynamic Raman enhancement.

Because the Raman scattering intensity contributed by the electromagnetic enhancement is proportional to the fourth power of the enhancement factor for the local field ($|E|^4$/$|E_0|^4$), the electric field distributions can be calculated by the finite

difference time domain (FDTD) solutions. Therefore, the contribution of electromagnetic enhancement to the SERS performance was investigated by FDTD simulating the electric field distributions of MXene nanosheets and MXene-based multiporous nanosheet stacking structure models. As shown in Figure 5a,b, we first constructed a single few-layer Nb_2C MXene nanosheet model with the size of 5.3 nm × 100 nm × 40 nm, which is composed of 10 layers of Nb_2C MXene nanosheets stacked with a layer spacing of 0.28 nm. Subsequently, based on the single few-layer Nb_2C MXene nanosheet model, the regular triangular intersecting and irregular intersecting Nb_2C MXene nanosheet models are constructed to represent the local morphology of MXene-based multiporous nanosheet stacking structures and shown in Figure 5c,d. The simulated electric field distributions demonstrate that the electromagnetic enhancement regions (Figures 5b and S14a) of single few-layer Nb_2C MXene nanosheets are all located at the edges of rectangular stacked nanosheets under the excitation TFSF sources of 532, 633, and 785 nm, and the enhancement factors of the highest electromagnetic enhanced regions on the xy cross section are all up to 10^2, while the electromagnetic enhancement regions (Figures 5c,d and S14b,c) of regular triangular intersecting and irregular intersecting Nb_2C MXene nanosheet models are located at the edges and intersections of MXene nanosheets, and the corresponding enhancement factors are all as high as 10^4. It can be clearly seen that the electromagnetic enhancement factor of regular triangular intersecting and irregular intersecting Nb_2C MXene nanosheets can be significantly improved by about 2 orders of magnitude compared to single few-layer Nb_2C MXene nanosheets. Similarly, the SERS enhancement mechanism of Ti_3C_2-based multiporous nanosheet stacking structures can be mainly attributed to the 2 orders of magnitude improvement in the electromagnetic enhancement factor caused by the intersection of Ti_3C_2 MXene nanosheets (Figure S15a−d). Separately, the electromagnetic enhancement factor of Ti_3C_2-based multiporous nanosheet stacking structures is about an order of magnitude lower than that of Nb_2C-based multiporous nanosheet stacking structures, which is consistent with the SERS performance of experimental Raman spectra. Moreover, whether the single few-layer MXene nanosheet model or these two intersecting MXene nanosheet models simulating multiporous nanosheet stacking structures, their electromagnetic enhancement can be effectively excited by the TFSF source with the entire visible region, which is consistent with the aforementioned results of Raman spectra.

The existence of intersecting MXene nanosheets on the surface of MXene-based multiporous nanosheet stacking structures can enhance the electromagnetic enhancement factor by about 2 orders of magnitude (Figure 5e), which is less than the experimental results in SERS EF with 3 orders of magnitude improvement. Therefore, the development in physical adsorption of MXene-based multiporous nanosheet stacking structures on MeB molecules was reasonably considered. The characterized ζ-potential and BET surface area indicate (Figures 5f and S15e) that the significantly increased specific surface area of multiporous nanosheet stacking structures can provide more adsorption sites for probe molecules, and the multiporous nanosheet stacking structures with surficial negative potential are conducive to attract molecules with positive charges such as MeB, collectively promoting the physical adsorption effect to
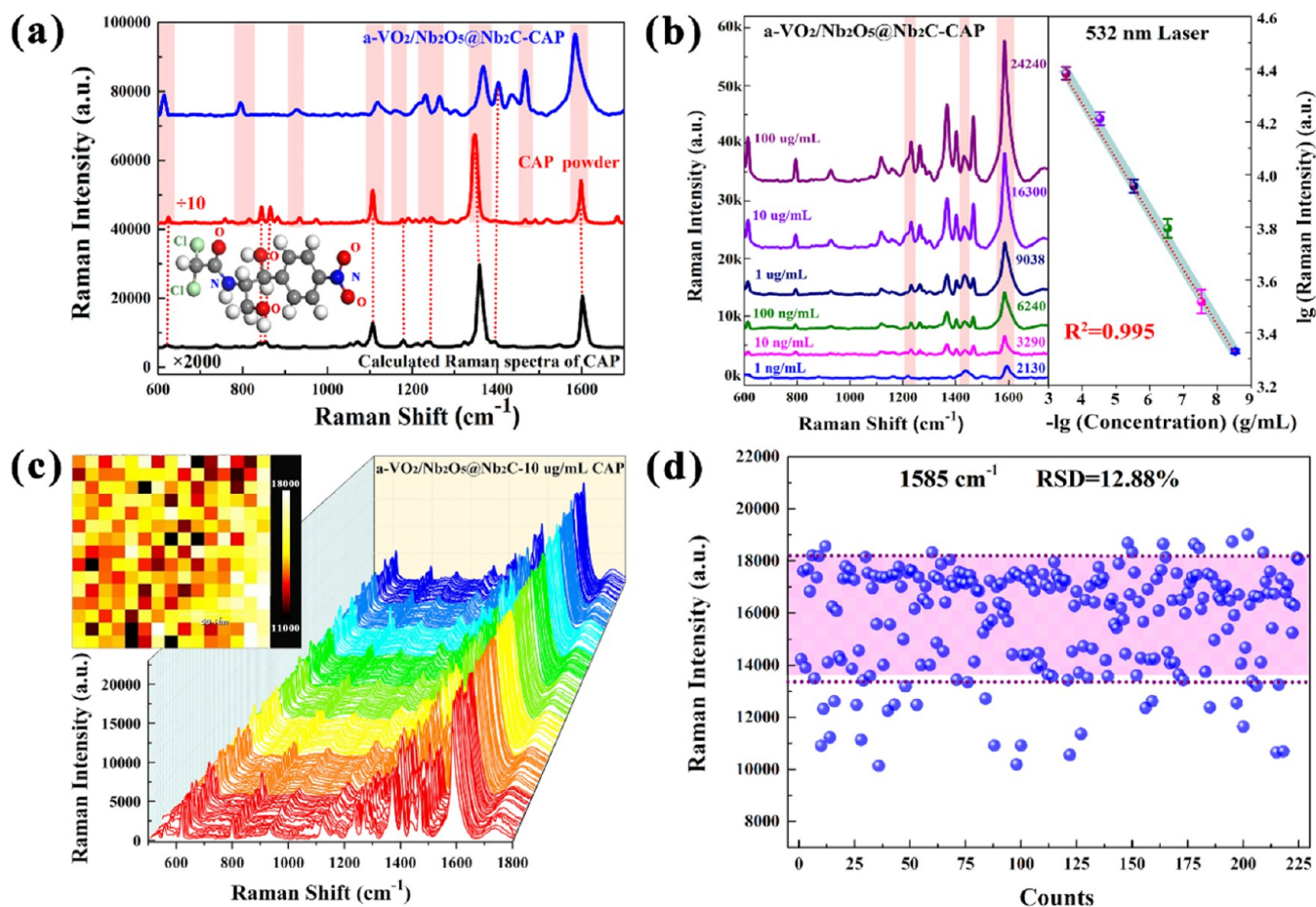
Figure 6. Ultrasensitive detection of CAP. (a) Comparison of Raman spectra of CAP on a-VO_2/Nb_2O_5@Nb_2C substrates, CAP powder, and calculated Raman spectra of the single CAP molecule. (b) Raman spectra and linear relationship between Raman intensity and molecular concentration of CAP with a concentration of 100 μg/mL on a-VO_2/Nb_2O_5@Nb_2C substrates. (c, d) Raman spectra and Raman mapping image (c) and the corresponding scatter plots of Raman intensity (d) at 1590 cm^{-1} of 10 μg/mL CAP on a-VO_2/Nb_2O_5@Nb_2C substrates. The step size is 10 μm.

develop its SERS performance. In conclusion, the SERS sensitivity of MXene-based multiporous nanosheet stacking structures is optimized by orders of magnitude under the multiple synergistic contributions of the developed physical adsorption, the chemical enhancement arising from the dynamic Raman enhancement, and the conspicuously improved electromagnetic enhancement originating from the intersecting MXene nanosheets.

2.6. SERS Detection of CAP

With the increasing abuse of antibiotic drugs, it is imperative to achieve normalized and portable detection of CAP in aquaculture and agricultural products due to its high toxicity. Motivated by the remarkably enhanced SERS sensitivity and the developed physical adsorption for molecules attributed to the high BET of Nb_2C-based multiporous nanosheet stacking structure substrates, Raman detection of the CAP antibiotic with a concentration of 100 μg/mL was conducted. The CAP molecule on a-VO_2/Nb_2O_5@Nb_2C substrates exhibits an obviously stronger Raman enhancement with the excitation laser of 532 nm than the other two excitation lasers of 633 and 785 nm (Figure S16). Under the optimal irradiation of the 532 nm laser, the characteristic Raman peaks of CAP located at Raman shifts of 1117, 1368, and 1585 cm^{-1} are significantly enhanced, which are assigned to the N−C stretching mode in the phenyl ring, the stretching vibration mode between an

electron-withdrawing group of nitro ($-NO_2$) with the phenyl ring, and the phenyl ring stretching mode of CAP, respectively. All these enhanced Raman peaks of CAP and their corresponding Raman vibration mode are listed in Table S3. In order to determine the accuracy of SERS-enhanced spectra of CAP on a-VO_2/Nb_2O_5@Nb_2C, theoretical Raman spectra of the isolated CAP molecule were calculated, and Raman spectra of CAP powder were directly detected. As shown in Figure 6a, the calculated Raman peaks and the directly detected Raman peaks of CAP powder match well with the Raman shifts of the CAP antibiotic enhanced by a-VO_2/Nb_2O_5@Nb_2C substrates, except for the difference in the Raman intensity caused by the synergistic SERS enhancement of CM and EM. Analysis results on LOD investigation (Figure 6b) indicate that a-VO_2/Nb_2O_5@Nb_2C substrates still exhibit a more excellent SERS enhancement on the CAP antibiotic with a low LOD of 1 ng/mL, which is beneficial to monitor the residual level of CAP in food-producing animals. The linear correlation between the intensity of the obviously enhanced characteristic Raman peak at 1585 cm^{-1} and the concentration of CAP ranging from 1 ng/mL to 100 μg/mL is satisfactory in logarithm with a correlation coefficient of 0.995. Furthermore, according to the Raman mapping of 10 μg/mL CAP on a-VO_2/Nb_2O_5@Nb_2C with 225 test points in an area of 150 × 150 μm^2 and its corresponding Raman intensity scatter plots at

1585 cm^{-1} (Figure 6c,d), the calculated RSD of 12.88% indicate the excellent uniformity of the enhanced effect for the Raman signal of CAP on a-VO$_2$/Nb$_2$O$_5$@Nb$_2$C. In a word, the developed Nb$_2$C-based multiporous nanosheet stacking structure with excellent detection sensitivity and SERS enhancement uniformity for CAP has a great promising perspective for the trace detection of other antibiotics in microsystems.

3. CONCLUSIONS

In summary, a universal optimization strategy of SERS performance that assembles few-layer MXene nanosheets into multiporous nanosheet stacking structures to improve the detection sensitivity of MXenes by orders of magnitude was innovatively proposed. The experimental key of this optimization strategy is incorporating NH$_4$VO$_3$ to induce the generation of amorphous oxides on the surface of MXenes, thus destroying the original van der Waals attraction that existed in the MXene nanosheet layers and further making the nanosheets intersect each other and forming multiporous nanosheet stacking structures. Taking Nb$_2$C MXene nanosheets as an example, the successfully synthesized multiporous nanosheet stacking structures are composed of Nb$_2$C MXene nanosheets with an average thickness of about 5.8 nm intersecting each other, and their phase structure is determined to be a-VO$_2$/Nb$_2$O$_5$@Nb$_2$C. With the optimal excitation laser of 633 nm, Nb$_2$C-based multiporous nanosheet stacking structures achieve ultrahigh detection sensitivity for MeB molecules with a low LOD of 10^{-10} M and a high EF of 2.6 × 10^9, which is improved by at least 3 orders of magnitude relative to few-layer Nb$_2$C MXene nanosheets. The SERS enhancement mechanism is mainly derived from the multiple synergistic contributions of the following three aspects: the increased BET surface area and the maintained surficial negative potential develop the physical adsorption capability, the existence of amorphous oxide on the MXene nanosheet surface promotes the dynamic chemical enhancement, and the intersecting MXene nanosheets can improve the electromagnetic enhanced factor by about 2 orders of magnitude. Furthermore, the few-layer Ti$_3$C$_2$ MXenes are applied as assembly templates to successfully synthesize Ti$_3$C$_2$-based multiporous nanosheet stacking structures with the SERS sensitivity optimized by 2 orders of magnitude, which verifies the universality of this SERS optimization strategy. Based on the developed Nb$_2$C-based multiporous nanosheet stacking structures, ultrasensitive detection of CAP with a wide linear range from 100 μg/mL to 1 ng/mL was achieved. It is believed that this developed SERS optimization strategy can be extended to other MXene materials with surficial negative charges through appropriate adjustment and provide a novel effective approach to conspicuously improve SERS sensitivity for the trace detection of other antibiotics in microsystems.

4. EXPERIMENTAL SECTION

4.1. Preparation of the MXene-Based Multiporous Nanosheet Stacking Structure

In this work, MXene-based multiporous nanosheet stacking structures were synthesized by the one-step hydrothermal reaction by adding ammonium metavanadate to the mixture of few-layer MXene nanosheets. First, we prepared few-layer MXene nanosheets as assembly templates of multiporous nanosheet stacking structures. Here, 3.0 g of Nb$_2$AlC powder or 2.0 g of Ti$_3$AlC$_2$ powder (Forsman Co., Ltd., Beijing, China) was dispersed in 50 mL of analytical

hydrofluoric acid (40 wt %, HF, Aladdin Co., Ltd., Shanghai, China) and electromagnetically stirred at room temperature for 14 days and 1 day, respectively. The etched products were centrifuged and washed with water and ethanol more than five times. The obtained clear multilayer Nb$_2$C or Ti$_3$C$_2$ MXene powder was dispersed in 60 mL of TPAOH solution and electromagnetically stirred for 3 days at room temperature, as well as washed with deionized water and absolute ethanol more than three times to obtain the exfoliated multilayer Nb$_2$C or Ti$_3$C$_2$ MXene black powder. Then, this exfoliated multilayer Nb$_2$C or Ti$_3$C$_2$ powder was evenly dispersed in 30 mL of deionized water, ultrasonically oscillated for 36 h in an ice bath, and then freeze-dried to obtain the black fluffy few-layer Nb$_2$C or Ti$_3$C$_2$ MXene nanosheet powder.

In the next hydrothermal reaction, 0.02 g of few-layer Nb$_2$C or 0.016 g of few-layer Ti$_3$C$_2$ MXene powder was dispersed into a mixed solution with a ratio of 30 mL/6 mL of deionized water and ammonia and ultrasonically vibrated for 20 min for uniform dispersion to obtain black mixed solution A. Simultaneously, 0.750 g of NH$_4$VO$_3$ was dissolved in 30 mL of deionized water and electromagnetically stirred for 30 min at 50 °C to obtain transparent solution B. Then, prepared black mixed solution A was added to transparent solution B and electromagnetically stirred for 20 min to mix evenly. The obtained precursor solution was transferred into a 100 mL hydrothermal reactor and hydrothermally reacted at 150 °C for 6 h to obtain gray and black fluffy precipitates. Finally, Nb$_2$C- or Ti$_3$C$_2$-based multiporous nanosheet stacking structure fluffy powder was obtained after centrifugation, washing, and freeze-drying.

4.2. Characterization and SERS Detection

The XRD spectra of few-layer Nb$_2$C and Ti$_3$C$_2$ MXene nanosheets and Nb$_2$C- and Ti$_3$C$_2$-based multiporous nanosheet stacking structures were obtained by a Rigaku D/MAX-2200 PC XRD system under the Kα radiation of Cu, a wavelength (λ) of 1.54 Å, and current and voltage of 40 mA and 40 kV, respectively. The micromorphology and phase structure of few-layer MXene nanosheets and MXene-based multiporous nanosheet stacking structures were characterized by an FEI Magellan 400 field emission scanning electron microscope (FESEM) and a JEM-2100F field emission source transmission electron microscope (200 kV) to obtain the SEM, TEM, HRTEM, EDS, and SAED images. The average thickness of few-layer Nb$_2$C and Ti$_3$C$_2$ MXene nanosheets was collected from AFM images measured by a Veeco DI Nanoscope MultiMode V system. A Thermo Fisher Scientific ESCAlab250 was used to provide the XPS spectra of few-layer MXene nanosheets and MXene-based multiporous nanosheet stacking structures.

Here, Raman detections of MeB molecules with concentrations of 10^{-6}−10^{-10} M and the CAP antibiotic with concentrations of 100 μg/mL−1 ng/mL were conducted based on MXene-based multiporous nanosheet stacking structures. First, about 0.01 g of product powder was added to 30 mL of MeB solutions and 10 mL of CAP solutions with different concentrations and ultrasonically mixed for 2 h. The bottom 10 μL of the mixture of molecules and substrates was collected and dropped on a glass slide after centrifugation and air-dried at room temperature to form a circle with a diameter of about 1 cm for the Raman test. All Raman spectra were measured by a Renishaw inVia Reflex Raman spectrometer with excitation lasers of 532, 633, and 780 nm. Laser powers were 50 mW × 1% for 532 nm, 17 mW × 1% for 633 nm, and 300 mW × 0.05% for 785 nm. The accumulation time was 20 s, and the laser beam was 50× microscope objective. At least three different points were tested on each molecule−substrate complex, and the Raman peak at 1620 cm^{-1} was selected to calculate the SERS EF value as well as to analyze the relationship trend between Raman intensity and MeB concentration.

4.3. Contribution of Amorphization to the SERS Activity of Nb$_2$C-Based Multiporous Nanosheet Stacking Structures Based on DFT Calculations

The first-principles calculations based on DFT[42] were employed to analyze the contribution of the existence of surficial amorphous oxides of V and Nb to the chemical enhancement in the SERS activity of

Nb$_2$C-based multiporous nanosheet stacking structures based on DFT calculations. First, the supercell expansion of $2 \times 2 \times 1$ for the Nb$_2$C MXene crystal structure was constructed, and then $-$O and $-$VO$_2$ groups were adsorbed on the surface of the supercell structure of Nb$_2$C MXenes to construct the amorphous adsorption models of Nb$_2$CO$_2$ and Nb$_2$CO$_2$V. After geometric optimization, the electronic structures, UV$-$vis absorption, and dielectric function spectra of Nb$_2$C MXenes and amorphous adsorption models Nb$_2$CO$_2$ and Nb$_2$CO$_2$V were calculated by the CASTEP program. During the calculation process, we adopted the PBE method in the generalized gradient approximation (GGA) to describe the periodic boundary conditions and the interelectronic exchange-correlation energy.[43] The interaction potential between the ion core and valence electrons was achieved by the ultrasoft potential (Ultrasoft). The cutoff energy of 500 eV in the wave vector K-space and the Brillouin zone of $7 \times 7 \times 1$ were chosen according to the special K-point of Monkhorst$-$Pack.[44] The outer electron configurations of the atomic pseudopotential calculation were $4d^45s^1$ for Nb, $3d^34s^2$ for V, $2s^22p^2$ for C, and $2s^22p^4$ for O, and the U values of Nb and V were both set to 3.0. The calculation accuracy of the crystal structure system reaching the convergence state was set as follows: the total energy change of the system was stable within 5×10^{-6} eV, the force acting on each atom in the unit cell was less than 0.01 eV/Å, and the residual stress of the unit cell and the tolerance deviation were 0.02 GPa and 10^{-3} Å, respectively.

Then, in order to directly analyze the influence of the existence of surficial amorphous oxides of V and Nb on their Raman enhancements, the complex models of MeB-Nb$_2$C, MeB-Nb$_2$CO$_2$, and MeB-Nb$_2$CO$_2$V were constructed to calculate the static Raman spectra by the Gauss09 program. Becke's three-parameter hybrid exchange functional and Lee, Yang, and Parr's (B3LYP) exchange functional combined with basis sets were adopted for all calculations. The probe molecules and cluster models were optimized without virtual frequencies to ensure keeping all structures in a stable state with the lowest energy. The 6-311+G(d,p) group including a polarization function and a diffusion function was selected for the C, H, O, N, and S atoms in the MeB molecule system. The transition metal Nb and V atoms were described by the Lanl2dz basic group.

4.4. Contribution of Electromagnetic Enhancement to the SERS Activity of MXene-Based Multiporous Nanosheet Stacking Structures Based on FDTD Simulations

The electric field distributions of few-layer MXene nanosheets and MXene-based multiporous nanosheet stacking structures were simulated by the FDTD solution and can obtain the SERS enhancing factor $|E|^4/|E_0|^4$ contributed by EM. This method provides a convenient and general approach for calculating the optical response of nanostructures of arbitrary geometry to an incident light wave. First, we constructed a single few-layer MXene nanosheet model with the size of 5.3 nm $\times$ 100 nm $\times$ 40 nm composed of 10 layers of MXene nanosheets stacked with a layer spacing of 0.28 nm. Then, the regular triangular intersecting and irregular intersecting MXene nanosheet models were constructed by the above few-layer MXene nanosheet model to simulate the local morphology of MXene-based multiporous nanosheet stacking structures. Among them, each layer of MXenes in this simulation was set as a two-dimensional conductor, and the electrical conductivity of Ti$_3$C$_2$ and Nb$_2$C was set as 0.5×10^6 and 1.33×10^6 $\Omega^{-1}\cdot$m^{-1}, respectively.[45] The Z-polarized TFSF sources of 532, 633, and 785 nm parallel to the normal to the MXene nanosheets were aligned to simulations. To obtain accurate results in the simulations, the Yee cell size was set to 2 nm $\times$ 2 nm $\times$ 0.1 nm, and an external medium of vacuum was used.

■ ASSOCIATED CONTENT

ⓢ Supporting Information

The Supporting Information is available free of charge at https://pubs.acs.org/doi/10.1021/jacsau.3c00758.

Experimental details on enhancement factor calculations; material synthesis; and characterization (Figures S1$-$S16 and Tables S1$-$S3) (PDF)

■ AUTHOR INFORMATION

Corresponding Authors

Zhengren Huang $-$ *State Key Laboratory of High-Performance Ceramics and Superfine Microstructures, Shanghai Institute of Ceramics, Chinese Academy of Sciences, Shanghai 200050, People's Republic of China;* Email: zhrhuang@mail.sic.ac.cn

Yong Yang $-$ *State Key Laboratory of High-Performance Ceramics and Superfine Microstructures, Shanghai Institute of Ceramics, Chinese Academy of Sciences, Shanghai 200050, People's Republic of China; Center of Materials Science and Optoelectronics Engineering, University of Chinese Academy of Sciences, Beijing 100049, People's Republic of China;* ⓞ orcid.org/0000-0001-8996-2182; Email: yangyong@mail.sic.ac.cn

Authors

Yusi Peng $-$ *State Key Laboratory of High-Performance Ceramics and Superfine Microstructures, Shanghai Institute of Ceramics, Chinese Academy of Sciences, Shanghai 200050, People's Republic of China; Center of Materials Science and Optoelectronics Engineering, University of Chinese Academy of Sciences, Beijing 100049, People's Republic of China;* ⓞ orcid.org/0000-0003-1711-9473

Lili Yang $-$ *College of Integrated Circuit Science and Engineering, Nanjing University of Posts and Telecommunications, Nanjing 210023, People's Republic of China*

Yanyan Li $-$ *State Key Laboratory of High-Performance Ceramics and Superfine Microstructures, Shanghai Institute of Ceramics, Chinese Academy of Sciences, Shanghai 200050, People's Republic of China; Center of Materials Science and Optoelectronics Engineering, University of Chinese Academy of Sciences, Beijing 100049, People's Republic of China; University of Chinese Academy of Sciences, Beijing 100049, People's Republic of China*

Weida Zhang $-$ *State Key Laboratory of High-Performance Ceramics and Superfine Microstructures, Shanghai Institute of Ceramics, Chinese Academy of Sciences, Shanghai 200050, People's Republic of China; Center of Materials Science and Optoelectronics Engineering, University of Chinese Academy of Sciences, Beijing 100049, People's Republic of China; University of Chinese Academy of Sciences, Beijing 100049, People's Republic of China*

Meimei Xu $-$ *State Key Laboratory of High-Performance Ceramics and Superfine Microstructures, Shanghai Institute of Ceramics, Chinese Academy of Sciences, Shanghai 200050, People's Republic of China; Center of Materials Science and Optoelectronics Engineering, University of Chinese Academy of Sciences, Beijing 100049, People's Republic of China; University of Chinese Academy of Sciences, Beijing 100049, People's Republic of China*

Chenglong Lin $-$ *State Key Laboratory of High-Performance Ceramics and Superfine Microstructures, Shanghai Institute of Ceramics, Chinese Academy of Sciences, Shanghai 200050, People's Republic of China; Center of Materials Science and Optoelectronics Engineering, University of Chinese Academy of Sciences, Beijing 100049, People's Republic of China;*

University of Chinese Academy of Sciences, Beijing 100049,
People's Republic of China

Jianjun Liu − *State Key Laboratory of High-Performance
Ceramics and Superfine Microstructures, Shanghai Institute
of Ceramics, Chinese Academy of Sciences, Shanghai 200050,
People's Republic of China;* orcid.org/0000-0003-2452-
6966

Complete contact information is available at:
https://pubs.acs.org/10.1021/jacsau.3c00758

■ REFERENCES

(1) Dong, S. L.; He, D.; Zhang, Q.; Huang, C. N.; Hu, Z. H.; Zhang, C. Y.; Nie, L.; Wang, K.; Luo, W.; Yu, J.; Tian, B.; Wu, W.; Chen, X.; Wang, F. B.; Hu, J.; Xiao, X. H. Early cancer detection by serum biomolecular fingerprinting spectroscopy with machine learning. *eLight* **2023**, *3*, 17.

(2) Nguyen, L. M.; Nguyen, N. T. T.; Nguyen, T. T. T.; Nguyen, T. T.; Nguyen, D. T. C.; Tran, T. V. Occurrence, toxicity and adsorptive removal of the chloramphenicol antibiotic in water: a review. *Environ. Chem. Lett.* **2022**, *20*, 1929−1963.

(3) Chen, J.; Zheng, J.; Zhao, K.; Deng, A.; Li, J. Electro-chemiluminescence resonance energy transfer system between nontoxic SnS₂ quantum dots and ultrathin Ag@Au nanosheets for chloramphenicol detection. *Chem. Eng. J.* **2020**, *392*, No. 123670.

(4) Ma, X.; Li, H.; Qiao, S.; Huang, C.; Liu, Q.; Shen, X.; Sun, C.; et al. A simple and rapid sensing strategy based on structure-switching signaling aptamers for the sensitive detection of chloramphenicol. *Food Chem.* **2020**, *302*, No. 125359.

(5) Barveen, N. R.; Wang, T. J.; Chang, Y. H. Photochemical synthesis of Au nanostars on PMMA films by ethanol action as flexible SERS substrates for in-situ detection of antibiotics on curved surfaces. *Chem. Eng. J.* **2022**, *431*, No. 134240. DOI: 10.1016/j.cej.2021.134240.

(6) Imran, M.; Habib, F. E.; Majeed, S.; Tawab, A.; Rauf, W.; Rahman, M.; Umer, M.; Iqbal, M. LC-MS/MS-based determination of chloramphenicol, thiamphenicol, florfenicol and florfenicol amine in poultry meat from the Punjab-Pakistan. *Food Addit. Contam., Part A* **2018**, *35*, 1530−1542.

(7) Xiao, D. F.; Jie, Z. S.; Ma, Z. Y.; Ying, Y.; Guo, X. Y.; Wen, Y.; Yang, H. F. Fabrication of homogeneous waffle-like silver composite substrate for Raman determination of trace chloramphenicol. *Microchim. Acta* **2020**, *187*, 593.

(8) Jiao, A. X.; Cui, Q. Q.; Li, S.; Li, H. S.; Xu, L. L.; Tian, Y.; Ma, H.; Zhang, M. Y.; Liu, D. M.; Chen, X. Aligned TiO₂ nanorod arrays decorated with closely interconnected Au/Ag nanoparticles: Near-infrared SERS active sensor for monitoring of antibiotic molecules in water. *Sens. Actuators, B* **2022**, *350*, No. 130848.

(9) Li, H. H.; Geng, W. H.; Zheng, Z. H.; Haruna, S. A.; Chen, Q. S. Flexible SERS sensor using AuNTs-assembled PDMS film coupled chemometric algorithms for rapid detection of chloramphenicol in food. *Food Chem.* **2023**, *418*, No. 135998.

(10) Liu, B.; Zheng, S. Y.; Li, H. T.; Xu, J. J.; Tang, H. Y.; Wang, Y.; Wang, Y. C.; Sun, F.; Zhao, X. W. Ultrasensitive and facile detection

of multiple trace antibiotics with magnetic nanoparticles and core-shell nanostar SERS nanotags. *Talanta* **2022**, *237*, 122955.

(11) Tu, J.; Wu, T.; Yu, Q.; Li, J. X.; Zheng, S.; Qi, K. Z.; Sun, G. H.; Xiao, R.; Wang, C. W. Introduction of multilayered magnetic core−dual shell SERS tags into lateral flow immunoassay: A highly stable and sensitive method for the simultaneous detection of multiple veterinary drugs in complex samples. *J. Hazard. Mater.* **2023**, *448*, No. 130912.

(12) Yu, H. K.; Peng, Y. S.; Yang, Y.; Li, Z. Y. Plasmon-enhanced light−matter interactions and applications. *npj Comput. Mater.* **2019**, *5*, 45.

(13) Yang, L. L.; Peng, Y. S.; Yang, Y.; Liu, J. J.; Huang, H. L.; Yu, B. H.; Zhao, J. M.; Lu, Y. L.; Huang, Z. R.; Li, Z. Y.; Lombardi, J. R. A Novel Ultra-Sensitive Semiconductor SERS Substrate Boosted by the Coupled Resonance Effect. *Adv. Sci.* **2019**, *6*, No. 1900310.

(14) Alessandri, I.; Lombardi, J. R. Enhanced Raman Scattering with Dielectrics. *Chem. Rev.* **2016**, *116*, 14921−14981.

(15) Li, M. Z.; Wei, Y. J.; Fan, X. C.; Li, G. Q.; Tang, X.; Xia, W. Q.; Hao, Q.; Qiu, T. VSe₂₋ₓOₓ@Pd Sensor for Operando Self-Monitoring of Palladium-Catalyzed Reactions. *JACS Au* **2023**, *3* (2), 468−475.

(16) Huang, W.; Hu, L.; Tang, Y.; Xie, Z.; Zhang, H. Recent advances in functional 2D MXene-based nanostructures for next-generation devices. *Adv. Funct. Mater.* **2020**, *30*, No. 2005223.

(17) Naguib, M.; Mochalin, V. N.; Barsoum, M. W.; Gogotsi, Y. 25th Anniversary Article: MXenes: A New Family of Two-Dimensional Materials. *Adv. Mater.* **2014**, *26*, 992−1005.

(18) Huang, W. C.; Ma, C. Y.; Li, C.; Zhang, Y.; Hu, L. P.; Chen, T. T.; Tang, Y. F.; Ju, J. F.; Zhang, H. Highly stable MXene (V₂CTx)-based harmonic pulse generation. *Nanophotonics* **2020**, *9*, 2577−2585.

(19) Kannan, P. K.; Shankar, P.; Blackman, C.; Chung, C. H. Recent Advances in 2D Inorganic Nanomaterials for SERS Sensing. *Adv. Mater.* **2019**, *31*, No. e1803432.

(20) Ding, H. M.; Li, Y. B.; Li, M.; Chen, K.; Liang, K.; Chen, G. X.; Lu, J.; Palisaitis, J.; Persson, P. O. A.; Eklund, P.; Hultman, L.; Du, S. Y.; Chai, Z. F.; Gogotsi, Y.; Huang, Q. Chemical scissor−mediated structural editing of layered transition metal carbides. *Science* **2023**, *379*, 1130−1135.

(21) Wang, C.; Xu, J. W.; Wang, Y. Z.; Song, Y. F.; Guo, J.; Huang, W. C.; Ge, Y. Q.; Hu, L. P.; Liu, J.; Zhang, H. MXene (Ti₂NTx): Synthesis, characteristics and application as a thermo-optical switcher for all-optical wavelength tuning laser. *Sci. China Mater.* **2021**, *64*, 259−265.

(22) Ye, Y. T.; Yi, W. C.; Liu, W.; Zhou, Y.; Bai, H.; Li, J. F.; Xi, G. C. Remarkable surface-enhanced Raman scattering of highly crystalline monolayer Ti₃C₂ nanosheets. *Sci. China Mater.* **2020**, *63*, 794−805.

(23) Soundiraraju, B.; George, B. K. Two-Dimensional Titanium Nitride (Ti₂N) MXene: Synthesis, Characterization, and Potential Application as Surface-Enhanced Raman Scattering Substrate. *ACS Nano* **2017**, *11*, 8892−8900.

(24) Peng, Y. S.; Lin, C. L.; Long, L.; Masaki, T.; Tang, M.; Yang, L. L.; Liu, J. J.; Huang, Z. R.; Li, Z. Y.; Luo, X. Y.; Lombardi, J. R.; Yang, Y. Charge-Transfer Resonance and Electromagnetic Enhancement Synergistically Enabling MXenes with Excellent SERS Sensitivity for SARS-CoV-2 S Protein Detection. *Nano−Micro Lett.* **2021**, *13*, 52.

(25) Peng, Y. S.; Cai, P.; Yang, L. L.; Liu, Y. Y.; Zhu, L. F.; Zhang, Q. Q.; Liu, J. J.; Huang, Z. R.; Yang, Y. Theoretical and Experimental Studies of Ti₃C₂ MXene for Surface-Enhanced Raman Spectroscopy-Based Sensing. *ACS Omega* **2020**, *5*, 26486−26496.

(26) Sarycheva, A.; Makaryan, T.; Maleski, K.; Satheeshkumar, E.; Melikyan, A.; Minassian, H.; Yoshimura, M.; Gogotsi, Y. Two-Dimensional Titanium Carbide (MXene) as Surface-Enhanced Raman Scattering Substrate. *J. Phys. Chem. C* **2017**, *121*, 19983−19988.

(27) Chen, K. Y.; Yan, X. H.; Li, J. K.; Jiao, T. F.; Cai, C.; Zou, G. D.; Wang, R.; Wang, M. L.; Zhang, L. X.; Peng, Q. M. Preparation of Self-Assembled Composite Films Constructed by Chemically-Modified MXene and Dyes with Surface-Enhanced Raman Scattering Characterization. *Nanomaterials* **2019**, *9*, 284.

(28) Aubrey, K. L.; Thomas, G. J. Raman spectroscopy of filamentous bacteriophage Ff (fd, M13, f1) incorporating specifically-deuterated alanine and tryptophan side chains. Assignments and structural interpretation. *Biophys. J.* **1991**, *60*, 1337−1349.

(29) Peng, Y. S.; Lin, C. L.; Tang, M.; Yang, L. L.; Yang, Y.; Liu, J. J.; Huang, Z. R.; Li, Z. Y. Niobium pentoxide ultra-thin nanosheets: A photocatalytic degradation and recyclable surface-enhanced Raman scattering substrate. *Appl. Surf. Sci.* **2020**, *509*, No. 145376.

(30) Ye, Z. W.; Li, C. C.; Celentano, M.; Lindley, M.; O'Reilly, T.; Greer, A. J.; Huang, Y. M.; Hardacre, C.; Haigh, S. J.; Xu, Y. K.; Bell, S. E. J. Surfactant-free Synthesis of Spiky Hollow Ag−Au Nanostars with Chemically Exposed Surfaces for Enhanced Catalysis and Single-Particle SERS. *JACS Au* **2022**, *2* (1), 178−187.

(31) Dai, Z. G.; Xiao, X. H.; Wu, W.; Zhang, Y. P.; Liao, L.; Guo, S. S.; Ying, J. J.; Shan, C. X.; Sun, M. T.; Jiang, C. Z. Plasmon-driven reaction controlled by the number of graphene layers and localized surface plasmon distribution during optical excitation. *Light Sci.: Appl.* **2015**, *4*, No. e342.

(32) Guan, H. M.; Yi, W. C.; Li, T.; Li, Y. H.; Li, J. F.; Bai, H.; Xi, G. C. General molten-salt route to three-dimensional porous transition metal nitrides as sensitive and stable Raman substrates. *Nat. Commun.* **2021**, *12*, No. 1376.

(33) Guan, H. M.; Yi, W. C.; Li, T.; Li, Y. H.; Li, J. F.; Bai, H.; Xi, G. C. Low temperature synthesis of plasmonic molybdenum nitride nanosheets for surface enhanced Raman scattering. *Nat. Commun.* **2020**, *11*, No. 3889.

(34) Ye, Y.; Chen, C.; Li, W.; Guo, X.; Yang, H.; Guan, H.; Bai, H.; Liu, W.; Xi, G. C. Highly Sensitive $W_{18}O_{49}$ Mesocrystal Raman Scattering Substrate with Large-Area Signal Uniformity. *Anal. Chem.* **2021**, *93*, 3138−3145.

(35) Du, R.; Yi, W.; Li, W.; Yang, H.; Bai, H.; Li, J.; Xi, G. C. Quasi-metal Microwave Route to MoN and Mo_2C Ultrafine Nanocrystalline Hollow Spheres as Surface-Enhanced Raman Scattering Substrates. *ACS Nano* **2020**, *14*, 13718−13726.

(36) Ji, W.; Li, L. F.; Guan, J.; Mu, M.; Song, W.; Sun, L.; Zhao, B.; Ozaki, Y. Hollow Multi-Shelled V_2O_5 Microstructures Integrating Multiple Synergistic Resonances for Enhanced Semiconductor SERS. *Adv. Opt. Mater.* **2021**, *9*, No. 2101866.

(37) Wang, X.; Guo, L. SERS Activity of Semiconductors: Crystalline and Amorphous Nanomaterials. *Angew. Chem., Int. Ed.* **2020**, *59*, 4231−4239.

(38) Wang, X. T.; Shi, W. X.; Jin, Z.; Huang, W. F.; Lin, J.; Ma, G. S.; Li, S. Z.; Guo, L. Remarkable SERS Activity Observed from Amorphous ZnO Nanocages. *Angew. Chem., Int. Ed.* **2017**, *56*, 9851−9855.

(39) Wang, X. T.; Shi, W. X.; Wang, S. X.; Zhao, H. W.; Lin, J.; Yang, Z.; Chen, M.; Guo, L. Two-Dimensional Amorphous TiO_2 Nanosheets Enabling High-Efficiency Photoinduced Charge Transfer for Excellent SERS Activity. *J. Am. Chem. Soc.* **2019**, *141*, 5856−5862.

(40) Kang, J. X.; Li, F. S.; Xu, Z. Y.; Chen, X. Y.; Sun, M. K.; Li, Y. H.; Yang, X. Y.; Guo, L. How Amorphous Nanomaterials Enhanced Electrocatalytic, SERS, and Mechanical Properties. *JACS Au* **2023**, *3* (10), 2660−2676.

(41) Ng, V. M. H.; Huang, H.; Zhou, K.; Lee, P. S.; Que, W. X.; Xu, Z. J.; Kong, L. B. Recent progress in layered transition metal carbides and/or nitrides (MXenes) and their composites: synthesis and applications. *J. Mater. Chem. A* **2017**, *5*, 8769.

(42) Hohenberg, P.; Kohn, W. Inhomogeneous Electron Gas. *Phys. Rev.* **1964**, *136*, B864−B871.

(43) Perdew, J. P.; Burke, K.; Ernzerhof, M. Generalized Gradient Approximation Made Simple. *Phys. Rev. Lett.* **1996**, *77*, 3865−3868.

(44) Monkhorst, H. J.; Pack, J. D. Special points for Brillouin-zone integrations. *Phys. Rev. B* **1976**, *13*, 5188−5192.

(45) Hu, C. F.; Li, F. Z.; He, L. F.; Liu, M. Y.; Zhang, J.; Wang, J. M.; Bao, Y. W.; Wang, J. Y.; Zhou, Y. C. In Situ Reaction Synthesis, Electrical and Thermal, and Mechanical Properties of Nb_4AlC_3. *J. Am. Ceram. Soc.* **2008**, *91*, 2258−2263.